Micro-Scale Modeling of Li-Ion Batteries: Parameterization and Validation

G. B. Less, J. H. Seo, S. Han, A. M. Sastry, J. Zausch, A. Latz, S. Schmidt, C. Wieser, D. Kehrwald and S. Fell

J. Electrochem. Soc. 2012, Volume 159, Issue 6, Pages A697-A704.
doi: 10.1149/2.096205jes

Journal of The Electrochemical Society, **159** (6) A697-A704 (2012)
0013-4651/2012/159(6)/A697/8/$28.00 © The Electrochemical Society

Micro-Scale Modeling of Li-Ion Batteries: Parameterization and Validation

G. B. Less,[a] J. H. Seo,[a] S. Han,[a] A. M. Sastry,[a,b,c,z] J. Zausch,[d,*] A. Latz,[d] S. Schmidt,[d] C. Wieser,[e] D. Kehrwald,[e] and S. Fell[e]

[a]*Department of Mechanical Engineering,* [b]*Department of Material Science and Engineering, and*
[c]*Department of Biomedical Engineering, University of Michigan, Ann Arbor, Michigan 48109, USA*
[d]*Fraunhofer Institute for Industrial Mathematics, 67663 Kaiserslautern, Germany*
[e]*GM Alternative Propulsion Center Europe, Adam Opel AG, IPC MK-01, 65423 Rüsselsheim, Germany*

A fully parameterized microscale model for lithium ion cells is presented in which the solid and pores (filled by electrolyte) are spatially resolved, and the mass and charge transport equations describing diffusion and migration in each phase are solved separately. Such a model allows: (1) the correlation of structure-scale, non-homogeneous material properties with macroscopic battery performance, and (2) the correlation of geometrical electrode morphology with macroscopic battery performance (electrode design). The micro-model approach discussed here allows for a simpler parameterization as fewer constitutive relations are needed in contrast to the macro-homogenous physical-based approaches. Input parameters were measured experimentally on lithium manganese oxide electrodes and $LiPF_6$ in 3:7 EC:DMC. Verification and validation for the model is also reported.
 [DOI: 10.1149/2.096205jes]

Manuscript submitted November 23, 2011; revised manuscript received February 21, 2012. Published March 22, 2012.

Since their first commercialization in the 1990s, Li-ion batteries have become an increasing part of the day-to-day life of consumers. Thanks to their relatively high energy and power densities, Li-ion batteries have enabled the development of miniaturized portable electronics, wireless communications devices, and lighter, more powerful cordless power tools. The next generation of Li-ion battery is being employed for larger scale applications such as power grid load leveling, stationary storage for solar and wind energy, and the electrification of vehicles. While it is important to have a firm understanding of the reliability and limitations of the Li-ion battery in all applications, this is especially true in vehicle applications where large cells and packs are in close proximity to the user.

As the demand for electrification increases, batteries will be expected to perform at even higher levels, coming closer to their theoretical limits. Currently, most battery chemistries and assembly methods are tested experimentally at all stages, from synthesis and cell assembly, through battery cycling. This process is costly in terms of raw materials, physical resources, and time. An alternative, less expensive approach is to use micro-scale modeling to numerically simulate the Li-ion batteries using fundamental parameters of the materials under study to predict the performance of the cell. The strengths of a micro scale model include: (1) Correlation of structure-scale, non-homogeneous material properties with macroscopic battery performance, (2) Correlation of geometrical electrode morphology with macroscopic battery performance (electrode design), (3) Understanding of degradation mechanisms due to changes of the geometrical morphology, changes of the intrinsic kinetic and/or transport properties of the individual phases. Additionally, in comparison to other modeling techniques which use a macro-homogeneous physical based approach, the parameterization of a micro model is relatively straightforward. There are no "mixture type" relations needed: only the intrinsic properties of the individual phases and interphases enter the equation set.

Micro-scale modeling considers the diffusion, conduction, and electrochemical kinetics of the electrodes at the micrometer scale, and can be used to simulate the electron transport and ion transport in the electrodes and separator of Li-ion batteries. In these models, the microstructure of the electrodes is resolved on the micrometer scale. On this scale the transport in the active particles and the electrolyte in between the particles has to be considered separately, as separate transport mechanisms are dominant in each of the two phases. The electrolyte ideally consists of a concentrated, fully-dissociated salt in solvent. The high salt concentration is the cause of a very short Debye screening length, which renders the electrolyte practically a charge-neutral system except for the double layer around the active particles. Due to the charge neutrality, the motion of positive and negative ions is highly correlated and, as in any electrolyte, charge and ion transport are strongly coupled. Ionic fluxes and electric currents are both caused by concentration gradients as well as by gradients in the electric potential.

In the active particles, charge and ion transport are much more decoupled. Electric currents are almost completely electronic in nature, due to the large mobility of electrons compared to that of ions. Conversely, ions are transported by diffusion only. The transport in electrolyte and active particles is coupled through the intercalation and deintercalation of ions into and from the active particles. Under ideal operating conditions, negative ions should not intercalate into active materials, nor should electrons diffuse into the electrolyte. The latter process is one of the many degradation mechanisms in Li-ion batteries. For a simulation algorithm to reliably predict the behavior of a Li-ion battery a sufficient number of parameters must be used, and the input values for those parameters must be accurate. Unfortunately, many of the parameters necessary to describe a functioning Li-ion battery vary widely in the literature. For example, experimental values of Li-ion diffusivity in lithium manganese oxide span four orders of magnitude (10^{-9}-10^{-12} cm^2s^{-1}) in the literature.[1–12] The value measured for Li-ion diffusivity can be affected by the synthesis method used for the active material (thin film vs. composite), the state of charge the measurement was taken at, and the measurement technique used to determine the diffusion coefficient.[9] This means that it is necessary to compile the input parameters for each specific battery prior to modeling. In previous electrode models[13] researchers found fully described cells in the literature, which afforded them sufficient parameters to develop a 3D mesoscale model of a Li-ion polymer cell. Alternatively, a database of realistic parameter ranges can be developed which allows the modeler to choose input values which are likely to afford realistic output values. This assures a broader range of applicable systems that can be modeled, as well as a more robust code. Parameters used in a cell model can be classified into four major categories: thermodynamic properties, electrode kinetic properties, transport properties, and electrode microstructural information. Driving forces for electrochemical reactions are determined by the thermodynamic properties of the electrodes and the electrolyte. The rate of the reactions at the electrode-electrolyte interface in response to this driving force depends on electrode kinetics parameters. Before electrochemical reactions can occur, ions and electrons must travel through the electrolyte and electrodes, respectively. Parameters

* Electrochemical Society Active Member.
z E-mail: amsastry@umich.edu

that describe movements of electroactive species in both the electrolyte and the electrodes can be classified as transport properties. Finally, the microstructure of electrodes can have a significant impact on cell performance. In thin-film batteries, the microstructure of electrodes is described by grain size distribution and grain boundary densities, whereas in bulk-type electrodes particle size distribution (PSD) and void gaps or porosities, describe the microstructure well.

Existing battery simulations range from continuum models[13–16] and low dimensionality porous models,[17–19] to simulations that employ multi-scale, multi-physics models of simplified electrode structures.[15,16] 3D spherical active particles in a regular/random array have been simulated in a half-cell configuration.[13] 2D circular particles in an interpenetrating-electrode microstructure, have been modeled and have shown better performance than the classical laminated electrode design.[14] 3D ellipsoidal particles have been configured for electrode microstructure and reduced-order modeling has been applied for scale-bridging and efficient macroscale simulation.[15,16] These continuum models have used finite element methods.1D, 2D and continuum models are faster than 3D models, but are focused on the macro-scale distribution of state variables (i.e., electric potentials and Li-ion concentrations) with effective transport properties which is dependent upon the 3D electrode microstructure. Using a realistic model allows for the simulation of local distributions of micro-variables such as ionic concentration, potential, etc., in 3D across the different phases of the battery structure (i.e., solid phase and electrolyte phase) at the cost of computational time. Accurate 3D modeling begins with an interrogation of the percolation statistics, ideal aspect ratios, and packing densities needed in order to form a continuous network in three dimensions—a necessary condition for a composite electrode for the particle morphologies under study.[20–35] The physics of percolation influences the formation and aspect ratios of larger aggregates[22] of particles; accurate 3D geometry and dimensionality of the aggregates yields a basis for developing predictive models that bridge the gap between chemical modeling and nanoparticle interaction.[36–38] Multi-scale/multiphysics modeling enables the interrogation of the disparate size (atomic to macro) and time (seconds to minutes) scales present in a battery system.

A microstructure resolved simulation of battery cells requires a fully 3D implementation of the coupled transport equations for active particles and electrolyte. The underlying partial differential equations turn out to be highly nonlinear; this is especially due to nonlinear kinetics at the interfaces between particles and the electrolyte. Nonlinear constitutive equations for fluxes appearing in conservation equations are very common in all flows of complex fluids. A particularly efficient method for solving complex flow problems is the locally conservative finite volume method. It is applied in highly nonlinear granular flow problems,[39,40] viscoelastic flow problems,[41] fiber suspension flow,[42] and particle suspension flow.[43] Finite volume methods are also very efficient in solving electro-hydrodynamic problems.[44]

The objectives of this paper are:

1. To introduce a model that incorporates realistic microstructures and uses a consistent set of input parameters, allowing the correlation of structure-scale, non-homogeneous material properties with macroscopic battery performance.
2. To validate this model using experimentally obtained results.

Methods

Model development.— The model used for our simulation is based on a thermodynamic consistent transport theory for the electrolyte,[45,46] a diffusion ansatz for Li-ion transport in the active particles, and Ohms law for the charge transport in the active particles. The intercalation and deintercalation of ions into and from the active particles uses a Butler Volmer ansatz for the current and the ion flux. The open circuit potential of the cathode and anode active particles (relative to the Li/Li^+ potential) as a function of the state of charge is input in the simulation of a full cell. In the current paper we concentrate on a half cell simulation with a lithium manganese spinel as the cathode material; however, the derived equation set is equally valid for other anode and cathode materials. The separator is treated as an effective electrolyte property. The aim is to resolve the transport processes on a material relevant scale (i.e., micrometer scale.) The processes in the double layer, which occur on a scale between 1 nm up to about 100 nm, are not explicitly simulated. The properties of the double layer determine the interface conditions between the electrolyte and the active particles. For example the charging process of the double layer is assumed to be instantaneous. Li-ions are not stored in the double layer but are instantaneously (on the time scale of the simulation) intercalated in the lattice structure of the active particles or released into the electrolyte. The interface conditions assure that neither electrons enter the electrolyte nor negative ions intercalate into the active particles. Charge neutrality of the electrolyte is explicitly used in the derivation of the electrolyte transport model and is thus guaranteed at every time step of the simulation. At the Li metal-electrolyte interface of the half cell we assume a Butler-Volmer expression for the deposition of Li-ions on the Li metal surface. The "open circuit" potential of the Li metal is zero by definition. The geometric model of the cathode is a simple random array of active particles which has a given constant overall porosity. Note that only active particles are resolved; neither binder nor conductive additives are modeled. The electronic current is therefore solely carried by the solid phase whose conductivity is considered as effective quantity of the mixture of carbon black and active particles.

The general transport model derived in[46] can be summarized as follows. Where necessary we indicate the alterations used in the present work in order to perform half-cell simulations. In both phases the conservation equation for the concentration c of Li-ions and the charge q are given in solid and electrolyte phase by

$$\frac{\partial c}{\partial t} = -\vec{\nabla}\vec{N}_+ \qquad [1]$$

$$\frac{\partial q}{\partial t} = -\vec{\nabla}\vec{j} \qquad [2]$$

The ionic flux $\vec{N}_+$ and the electric current density $\vec{j}$ in the electrolyte be written as

$$\vec{N}_+ = -D_e\vec{\nabla}c + \frac{t_+}{Fz_+}\vec{j} \qquad [3]$$

$$\vec{j} = -\kappa\vec{\nabla}\phi - \kappa\frac{t_+}{Fz_+}\left(\frac{\partial\mu_+}{\partial c}\right)\vec{\nabla}c \qquad [4]$$

These expressions are valid in both phases; however, t_+ is zero in the solid phase, and therefore is used only for the electrolyte phase. The transport coefficients D_e, κ, t_+ are the interdiffusion coefficient of ions in the mixture of dissociated salt and solvent, the ionic conductivity, and the transfer coefficient of Li-ions, respectively. All transport coefficients may depend on the concentration of ions and the local electrical potential Φ. The charge of the positive ions is z_+ i.e. $z_+ = 1$ for Li-ions. The chemical potential of the Li-ions in the electrolyte is μ_+ and may be defined by $\mu_+ = RT\log(f_\pm c) + \mu_0$. F and $f_\pm$ are the Faraday number and the activity coefficient, respectively. The ionic flux and the electric current in the active particles are given by

$$\vec{N}_s = -D_s\vec{\nabla}c \qquad [5]$$

$$\vec{j} = -\sigma\vec{\nabla}\phi \qquad [6]$$

D_s, σ are the diffusion coefficient of ions in the active particles and the electronic conductivity of the active particles, respectively.

The intercalation of the ions in the active particles is modeled with the help of appropriate interface conditions. The rate of intercalation is commonly described with a Butler-Volmer expression i_{se} with

$$i_{se} = i_0\left(\exp\left(\frac{\alpha_a F}{RT}\eta_s\right) - \exp\left(-\frac{\alpha_c F}{RT}\eta_s\right)\right) \qquad [7]$$

and i_0, the exchange current density, is defined as

$$i_0 = k c_c^{\alpha_a} c_s^{\alpha_a} \left(1 - \frac{c_s}{c_{s,max}}\right)^{\alpha_c} \quad [8]$$

where $\eta_s = \phi_s - \phi_e - U_0(c_s)$ is the overpotential defined relative to the open circuit potential U_0. The relative strength of the anodic and cathodic reaction are α_a, α_c, respectively, where $\alpha_a + \alpha_c = 1$. We generally choose $\alpha_a = \alpha_c = 0.5$. c_e and c_s are the lithium ion concentrations on the electrolyte and solid sides of the interface, respectively. The maximum possible concentration of Li-ions in the active particle is $c_{s,\max}$. The proportionality factor k has to be determined experimentally. The rate i_{se} determines the ion flux as well as the electric current which is only due to the transport of Li-ions through the double layer (with subscript *se* denoting the current density between the solid and electrolyte.). As a consequence, we have at the interface between electrolyte and active particles

$$\vec{j}_s \vec{n} = \vec{j}_e \vec{n} \quad [9]$$

$$\vec{j}_s \vec{n} = i_{se} \quad [10]$$

$$\vec{N}_{+,s} \vec{n} = \vec{N}_{+,e} \vec{n} \quad [11]$$

$$\vec{N}_{+,s} \vec{n} = \frac{i_{se}}{F z_+} \quad [12]$$

The vector $\vec{n}$ is the normal pointing from the active particle toward the electrolyte. With the help of the four interface conditions the values of the electrical potentials and the concentrations on the electrolyte and particle side of the interface are obtained. The interface to the Li metal in the half cell is similarly treated. The only differences are the open circuit potential, which is set to zero for the Li metal and the choice of $i_0 = k\sqrt{c_e}$.

As boundary conditions we impose a zero potential at the Li foil and prescribe a given external current density at the external boundary of the cathode. Periodic boundary conditions are chosen for the side walls perpendicular to the cathode and anode surfaces.

To solve the coupled set of nonlinear partial differential equations we developed and implemented a cell-centered, fully implicit, finite volume discretization on polygonal meshes. The strong nonlinearities are treated with a Newton method analogous to the work of Popov et al.[47] The Jacobians of the Newton iteration are calculated analytically. For each time step about 3–4 Newton iterations are necessary to obtain convergence. To solve the discretized set of coupled non-linear equations, we use the Scientific Computation toolkit PETSc and the algebraic multigrid solver SAMG developed by Fraunhofer SCAI. For our simulations we used up to 200000 volume elements. The equations were solved on a standard multicore computer (Dell PowerEdge 1950, dual quad-core Intel Xeon E5420 (2.5 GHz), 16 GB RAM).

Two simulations were run to verify the model. The first simulation was of the OCV curve and used three different generic electrode geometries made of cubic particles. We used two random configurations and one non-random configuration with the same active volume but lower interfacial area, as seen in Figure 1. In the simulated cells, the total size was $40 \times 20 \times 20$ voxels, with each voxel representing a cube of 2.5 μm^3. The simulated electrodes had 60% porosity and a theoretical capacity of 23.79 nAh. The electrodes were set to an initial depth-of-discharge of 87% (i.e. x = 0.13 in $Li_xMn_2O_4$) and then galvanostatically charged at 1C, C/2, and C/4 until either a depth-of-discharge of 32% (x = 0.68) was achieved or the cell potential crossed 4.4V (whichever came first).

In the second simulated case study, we compared the results of a 1C charging of an LMO half cell with the corresponding experiment. In order to use a more realistic electrode geometry, a $100 \times 100 \times 100$ $(\mu m)^3$ volume of LMO particles was constructed based on the FIB-SEM image of Figure 4. The resulting simulation geometry is shown in Figure 11.

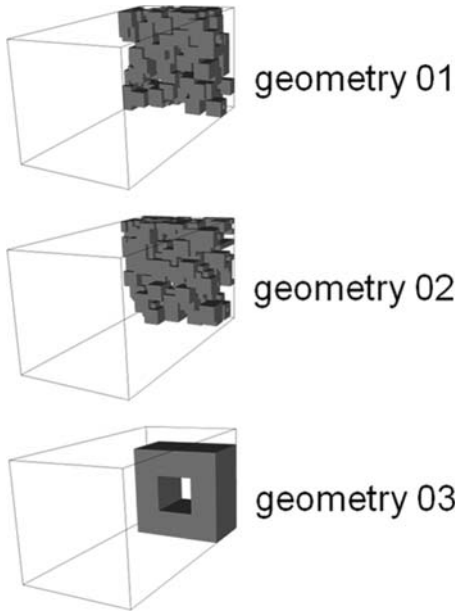

Figure 1. Simulation geometries used in the verification experiments.

Experimental methods.— All reagents were used as-received from Sigma-Aldrich chemical company, unless otherwise noted. Generally, Li-ion half cells were constructed for parameterization and validation purposes in an Ar atmosphere glove box (<1 ppm O_2 and H_2O) using a Swagelok. The anode—0.38 mm thick metallic lithium foil—was mounted on a copper current collector (110 Copper, 53 μm thick McMaster-Carr); Celgard 2325 was employed as the separator; the electrolyte was 1.2M $LiPF_6$ in 3:7 EC:DMC; a laminated composite electrode of composition 90 : 5 : 5 lithium manganese oxide : carbon black : binder (Kureha 7208 PVdF) was used as the cathode. A typical cathode was made by mixing 1.9999 g of lithium manganese oxide and 0.1100 g of carbon black at 3000 rpm for 1 min in a Speedmixer DAC 150 FVZ double centrifugal mixer using the MAX 10 adaptor. PVdF resin (1.6041 g) was then added and the slurry was mixed at 3000 rpm for 30 sec. The viscosity of the final slurry was adjusted by the addition of 2.15 g of NMP in three aliquots, with 30 sec. of mixing at 3000 rpm after each addition. A final homogenization and deaeration of the sample was performed by mixing the slurry for 2.5 minutes at 3000 rpm prior to casting. The cathode slurry was cast on an aluminum current collector (1100 Aluminum, 25 μm thick, McMaster-Carr) by hand with a 20 mil gap blade applicator. The cast electrode was dried *en vacuo* at 110°C overnight to assure complete solvent removal. The final dry thickness of the cathode was 49 μm, with a calculated porosity of 56%. For Swagelok cells the cathode is punched to form a 6.35 mm diameter electrode, and the anode is punched to form 8 mm disks. Electrochemical measurements were carried out using a Biologic VMP3 with an EIS module unless otherwise noted.

Electronic conductivity of the composite cathode films was measured with a Lucas Labs S-302-4 four-point probe. CV scans of the samples were run using GPES Manager in Autolab. The sample was scanned from −0.2 – 0.2 V using a step potential of 0.0025 V with a scan rate of 0.025 V/s. The sample was measured five times and the results averaged. In calculating the electronic conductivity of the sample, σ_e, 4.532 was used as the standard correction factor. Li^+ diffusivity in $LiMn_2O_4$ is determined by three different electrochemical techniques, namely, potentiostatic intermittent titration technique (PITT), galvanostatic intermittent titration technique (GITT), and electrochemical impedance spectroscopy (EIS). Measurements were taken on a bulk composite electrode fabricated as described and assembled in a typical Swagelok-type cell. For the PITT method, the long-time solution is used.[48] For the GITT method, the short-time

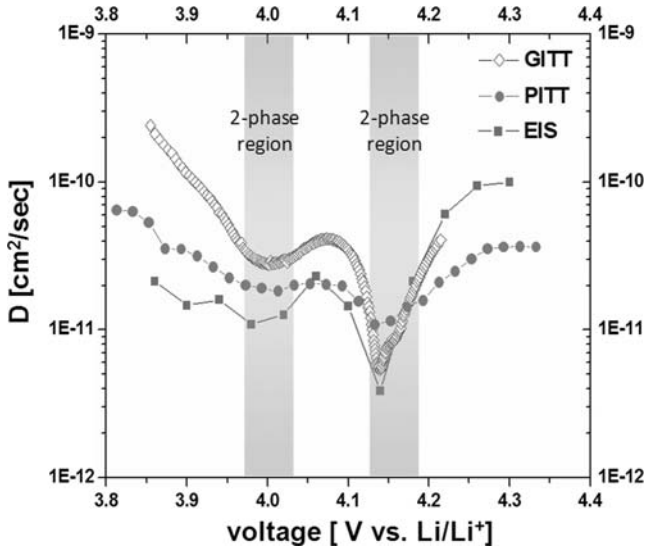

Figure 2. Li^+ diffusivity in lithium manganese oxide as a function of voltage. Due to the limitations and assumptions inherent in each of the measurement techniques used, the measured diffusion constant is a function of the methodology used for the measurement.

solution is used.[49] For the EIS method, a modified Randolph equivalent circuit is used to calculate diffusion coefficients.[50] All three electrochemical techniques used require interfacial surface area between the electrolyte and the electrode. The surface area is estimated by assuming a monodisperse spherical particle distribution within the porous bulk composite electrode. The results for all three diffusion techniques are shown in Figure 2. The open circuit voltage (OCV), shown in Figure 3, was determined experimentally by charging and discharging an LMO half cell with a C-rate of C/50. The mean particle size of the cathode active material was determined by FIB SEM microscopy (Figure 4).

1.2 M $LiPF_6$ in EC:DMC (3:7 v/v) was selected as the electrolyte. The following four parameters were used to characterize the transport properties of the electrolyte: (i) the ionic conductivity, κ, (ii) the diffusion coefficient, D, (iii) the Li^+ transference number, t_+^0, and (iv) the mean molar activity coefficient, $f_\pm$. These values were determined experimentally as a function of Li^+ concentration, except in the case of mean molar activity coefficient, where a constant value from the literature is used, since a sensitivity analysis showed low impact from this parameter on simulation results. The value used in the model for the mean molar activity coefficient of the electrolyte is actually the derivative with respect to the Li^+ concentration; thus, a constant was employed.

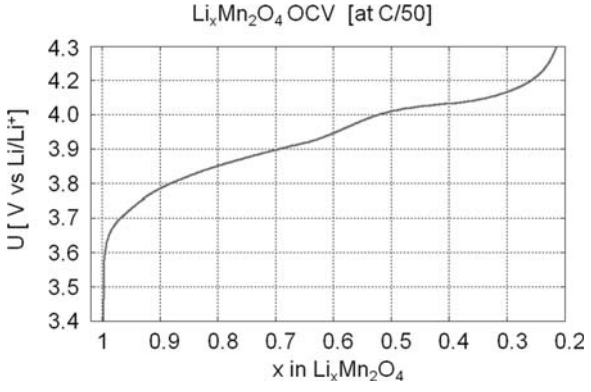

Figure 3. Open circuit voltage of lithium manganese oxide collected at a discharge rate of C/50 in a Swagelok-type cell.

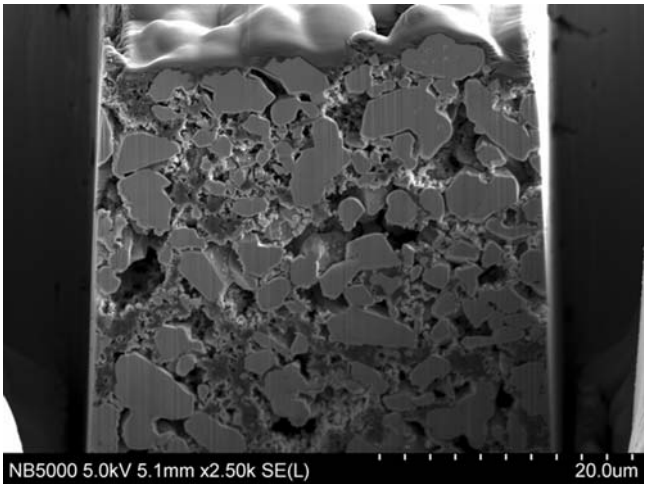

Figure 4. FIB-SEM micrograph of a lithium manganese oxide composite electrode.

The ionic conductivity of the electrolyte was measured in a symmetrical two-electrode Swagelok cell using electrochemical impedance spectroscopy (EIS). Blocking electrodes of stainless steel (grade 316) were used. Impedance was measured at frequencies from 10 mHz to 1 MHz, with 7.0 mV peak-to-peak amplitude. To control the electrolyte thickness and cross-sectional area, a Teflon spacer ring (8.86 mm inner diameter, 0.76 mm thickness) was used. A NaCl reference solution (Sigma-Aldrich) of known ionic conductivity was used to obtain the cell constant. The ionic conductivity is calculated from the real axis intercept in the high frequency range of the Nyquist plot. The ionic conductivity is calculated as a function of the $LiPF_6$ salt concentration from 0.2 M to 1.6 M (Table IV), and the data is fitted with a third-order polynomial (Figure 5).

The diffusion coefficients, D_{Li} and D_F, were measured using the nuclear magnetic resonance pulsed field gradient technique (NMR-pfg). The electrolyte was placed into a Wilmad 5 mm low pressure/vacuum NMR tube equipped with a PTFE stopper prior to removal from the glove box. The sample was analyzed on a Varian MR400, 400 MHz NMR using the dgcsteSL_cc sequence (DOSY Gradient Compensated Stimulated Echo with Spin Lock and Convection Compensation) that came with the DOSY package of Varian's Vnmrj 2.3 A. The Vnmrj

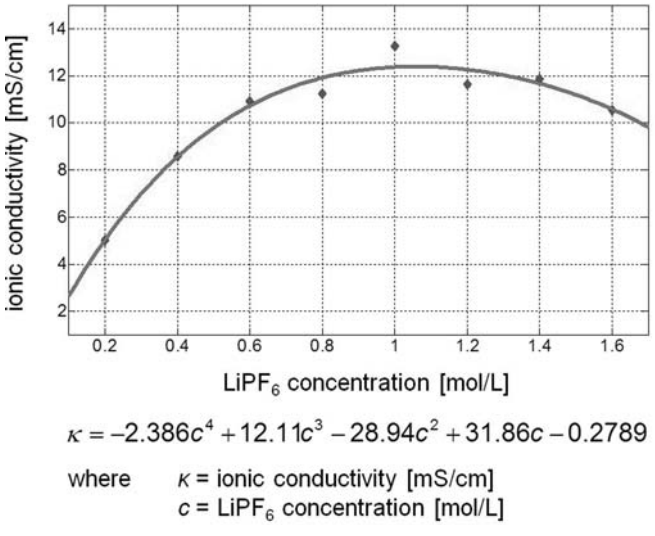

Figure 5. Ionic conductivity of lithium as a function of $LiPF_6$ concentration in a 3:7 EC:DMC solvent system.

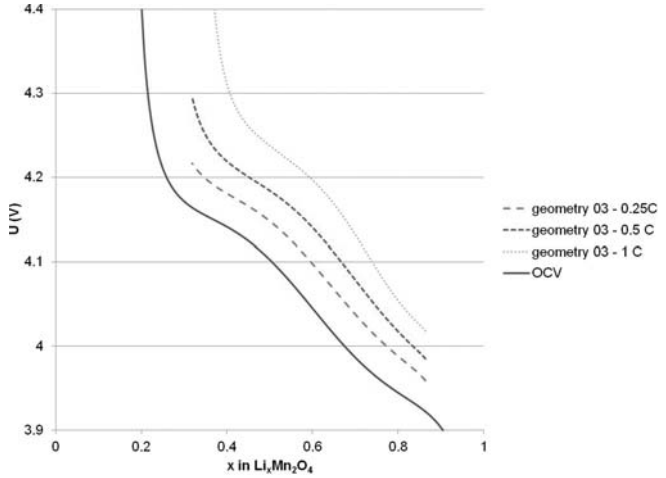

Figure 6. Simulation of various charge rates for geometry 03 as compared to the open circuit potential of LMO.

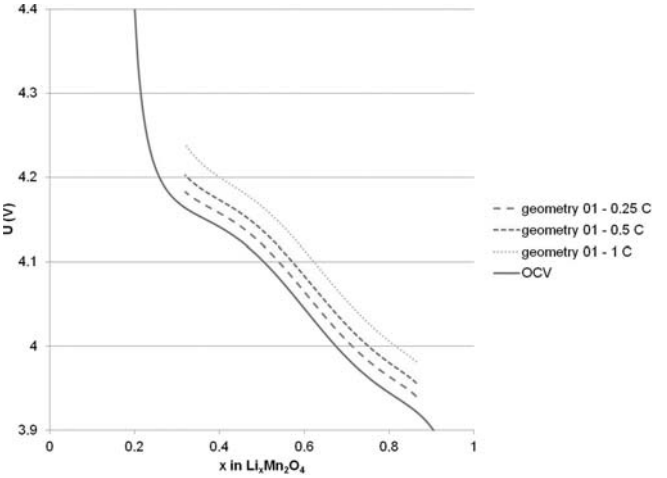

Figure 7. Simulation of various charge rates for geometry 01 as compared to the open circuit potential of LMO.

software was likewise used to calculate the diffusion coefficients from the resulting 15 pulse arrays. From the diffusion coefficients the Li-ion transference number was calculated using

$$t_{Li} = \frac{D_{Li}}{D_{Li} + D_F} \quad [13]$$

The interdiffusion coefficient was estimated by

$$D_e = \frac{c_F}{c_{Li} + c_F} D_{Li} + \frac{c_{Li}}{c_{Li} + c_F} D_F \quad [14]$$

where c_F and c_{Li} are the molar concentrations of the respective ions. The lithium diffusion constants are summarized in Table V.

To verify the model, two cells were made as described and cycled at $\pm$1C for comparison to simulated results.

Results

In case study 1 we perform simulations on three different generic geometries (Figure 1). We can see in Figures 6–8 that the simulated charging cycles tend to a higher voltage with increasing C-rate and all C-rates correspond to a higher voltage prediction than OCP, thus properly demonstrating the effect of over-potential. It is expected that during discharge we would see a similar decrease in cell voltage with increasing C-rate. Figure 9 shows the influence of cathode geometry/electrode-electrolyte interfacial surface area on over-potential; the simulations using geometries 01 and 02 exhibit a lower maximum cell potential than the simulation using geometry 03. The calculated surface areas of the three simulated geometries are as follows: geometry 01 = 16.7e^{-5} cm^2, geometry 02 = 15.7e^{-5} cm^{2,} and geometry 03 = 7.7e^{-5} cm^2. The lower electrode-electrolyte interfacial surface area of geometry 03 creates a diffusion limitation relative to the higher interfacial surface areas of the two random geometries modeled. This diffusion limitation in turn increases the potential of this sample in the simulated charging curve.

In case study 2 we perform simulations on the realistic electrode structure (Figure 4 and Figure 11). In Figure 10, the 1C charge voltage is plotted versus charging time for two experimental cells and the corresponding simulation. The simulated curve diverges at approximately 1750s, while the experimental charging times are in the range of 2500s and 3000s.

The simulation snapshot in Figure 11a shows the LMO lithium concentration at time t = 1750s. The red areas correspond to the initial (maximum) concentration in LMO. It is clear that there exist large concentration gradients within the particles. In the centers, the concentration is still almost at the initial value while the surface concentration is already reduced to about 25%. It is the surface con-

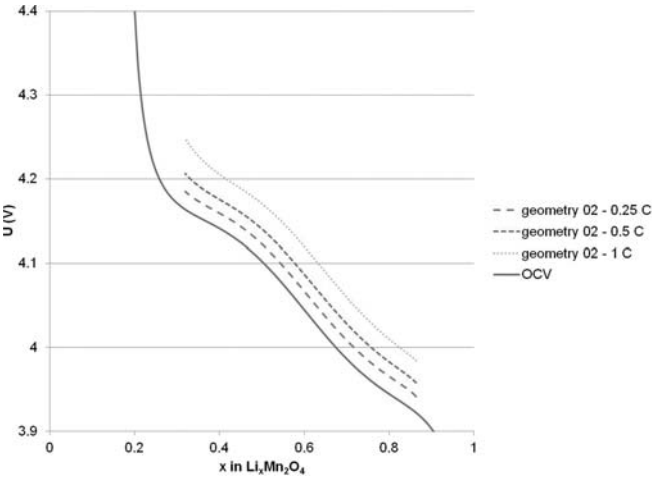

Figure 8. Simulation of various charge rates for geometry 02 as compared to the open circuit potential of LMO.

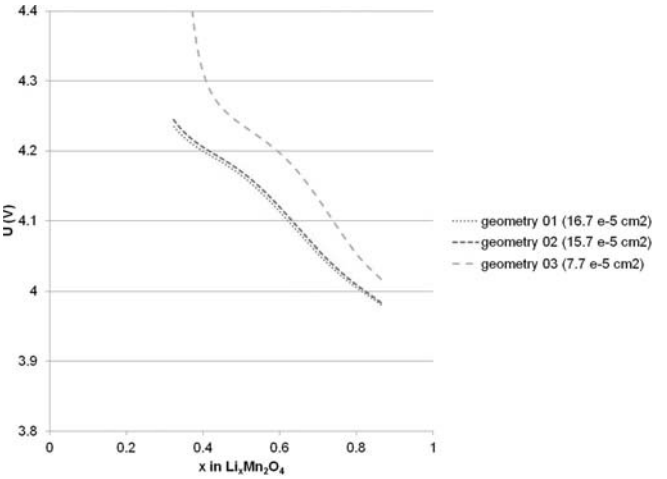

Figure 9. Comparison of the simulated 1C charge cycles for the three different geometries modeled (Figure 1).

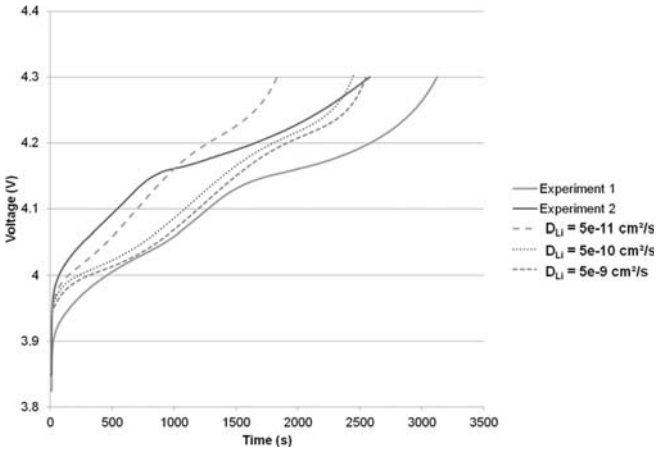

Figure 10. Experimental versus simulated charge cycle plotted as cell potential versus cycle time. Simulation results are plotted using the experimentally determined diffusion constant of 5e-11 cm^2/s as well as 5e-10 cm^2/s and 5e-9 cm^2/s in order to demonstrate the diffusion constant's strong influence in this setup.

centration entering the OCV-function which in turn determines the "measured" potential in the solid. While there are still plenty of ions left in the cathode, the particle surfaces become depleted and the potential must rise. It would seem that a relatively low LMO diffusion constant for the studied material ($5e^{-11}$ cm^2/s) is mainly responsible for the observed behavior. In order to demonstrate that it is indeed the low diffusion constant that makes the charging of the simulated battery stop much earlier than expected (at 1750s instead of 3600s), the simulation was re-run with two higher LMO diffusion constants. While the diffusion rate was $5e^{-11}$ cm^2/s in the original simulation, we increased it to $5e^{-10}$ cm^2/s and $5e^{-9}$ cm^2/s in the new runs to test our hypothesis. With higher diffusion constants the voltage curve diverges much later than before (Figure 10). The difference between the original and $5e^{-10}$ cm^2/s is very pronounced, while the difference of the results for the two highest diffusion constants is small. This means that at $D = 5e^{-10}$ cm^2/s the cell performance is no longer limited by the solid diffusion. Comparing the simulation snapshot pictures in Figure 11, all taken at the same time step (t = 1750s), we see that the concentration gradient within the active particles is much less with

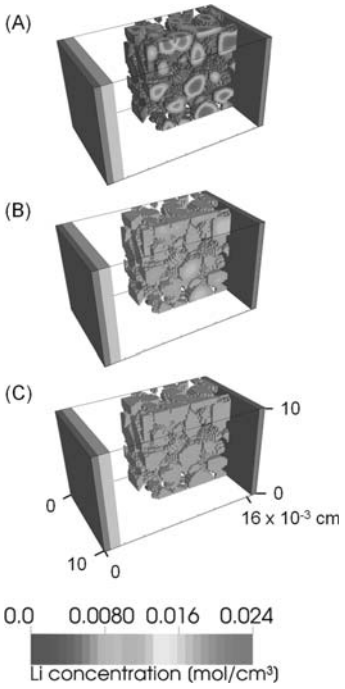

Figure 11. Simulation snap shots of the internal lithium concentration of the cathode materials at t = 1750s for (A) $D_{Li+} = 5e^{-11}$ cm^2/s, (B) $D_{Li+} = 5e^{-10} cm^2/s$, and(C) $D_{Li+} = 5e^{-9}$ cm^2/s. At diffusion constants greater than $5e^{-10}$ cm^2/s, the cell performance is no longer limited by solid diffusion.

the higher diffusion constant, and also that ions in the particle center can "participate" in the transport, thus leading to an enhancement of capacity.

The simulations still stop short of the expected 3600s required for a 1C charge. The cell capacity (and therefore the C-rate) is determined by the theoretical capacity of the simulated volume of LMO. The simulated OCV begins to diverge at approximately x = 0.2, suggesting we can only achieve about 80% of the theoretical capacity.

Results for the parameterization experiments are summarized in Tables I–V below.

Table I. Cathode input parameters, techniques used to determine their values, and the values found.

Variable Name	Transport Equation Variable	Technique Used	Value
cathode material	–		LMO
cathode current collector	–		1100 Al
cathode electron conductivity	σ_+	4 point probe	16.1 ± 2.04 S/m
cathode current collector conductivity	–	literature[54]	$3.69e^7$ S/m
cathode Li diffusivity	D_{s+}	EIS, PITT, GITT	Figure 2
maximum lithiation of cathode	–	calculated	23,671 mol/m^3
cathode OCV	–	CC discharge	Figure 3
cathode reaction coefficient/ proportionality factor	α_+	literature[18]	0.5
cathode mean particle size	–	FIB SEM	2.5 mm (Figure 4)

Table II. Anode input parameters, techniques used to determine their values, and the values found.

Variable Name	Transport Equation Variable	Technique Used	Value
anode material	–		lithium foil
anode current collector	–		110 copper
anode electron conductivity	σ_-	literature[54]	$1.06e^7$ S/m
anode current collector conductivity	–	literature[54]	$3.69e^7$ S/m
anode OCV	–	NA	0 V
anode reaction coefficient/ proportionality factor	α_-	literature[18]	0.5

Table III. Electrolyte and separator input parameters, techniques used to determine their values, and the values found.

Variable Name	Transport Equation Variable	Technique Used	Value
electrolyte	–	–	1.2 M $LiPF_6$ in 3:7 EC:DMC
transference number of Li^+	f_+	NMR	0.4
transference number of PF_6^-	f_-	NMR	0.6
ion conductivity of electrolyte	κ	EIS	Table IV + Figure 5
diffusion coefficient of Li^+ in electrolyte	D_e	NMR	Table V
separator porosity	–	literature[55]	0.39
separator thickness	–	literature[55]	20 mm

Table IV. Ionic conductivity of lithium as a function of $LiPF_6$ concentration in a 3:7 EC:DMC solvent system – see Figure 5.

x M $LiPF_6$ in EC:DMC (3:7 v/v)	ionic conductivity (mS/cm)
0.2 M	5.009 ± 0.011
0.4 M	8.572 ± 0.128
0.6 M	10.921 ± 0.058
0.8 M	11.239 ± 0.074
1.0 M	13.259 ± 0.076
1.2 M	11.639 ± 0.306
1.4 M	11.862 ± 0.145
1.6 M	10.535 ± 0.070

Table V. Lithium ion diffusion coefficient as a function of $LiPF_6$ concentration in 3:7 EC:DMC at 25°C as measured by NMR.

Concentration (moles/L)	D_{Li+} (m^2/sec)
0.4	$4.42e^{-10}$
0.6	$2.37e^{-10}$
0.8	$2.15e^{-10}$
1	$2.25e^{-10}$
1.2	$1.62e^{-10}$

Discussion

In comparing the 1C voltage curves a discrepancy is found not only between the simulated and experimental capacities but also between the two experimental curves, though this latter discrepancy is less pronounced. The former discrepancy is explained by the different definitions used for the capacity: while the simulation employs the theoretical capacity as basis for the magnitude of the 1C current, the experiment used the formation cycle to determine the cell capacity. As explained above, we can expect to achieve a maximum of only 80% of the theoretical capacity. This is in accordance with the result of experiment 2, where the cutoff voltage of 4.3 V is reached in the simulation at a time which is about 80% of the corresponding time in experiment 2. Furthermore, differences in the cell internal resistances will give non-identical discharge curves.

If these differences were not present, all three curves should lie on top of each other. In order to compare the shapes of the voltage curves better in Figure 12, we rescale time for each dataset individually such that all three curves reach the voltage of 4.3 V at the same point. However, we still cannot expect that all curves will now fall onto one master curve, since the absolute magnitude of the 1C current density was different in all three cases. Therefore, the overpotentials are different, which results in a vertical shift of the cell voltage. From this figure we conclude that the simulation is capable of producing data within experimental accuracy, although further fine-tuning is needed to match theoretical and experimental cell capacities. For example, one could use a scaling factor that relates the theoretical specific capacity

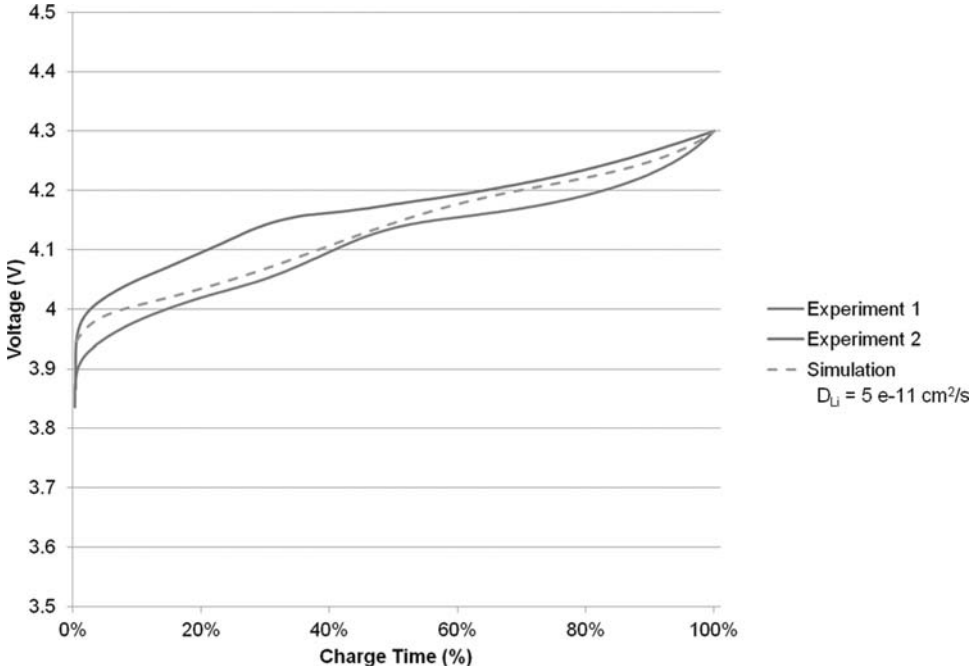

Figure 12. Experimental versus simulated charge cycle plotted as voltage versus the percent completion of the charge cycle. Note that this is the same data as Figure 10, rescaled to percent charge time.

to the experimental one. This way the absolute value of the simulated 1C current is lower and the voltage curve would be stretched to larger times.

The modeling approach presented here makes use of some simplifications. Firstly, when resolving the microstructure, only active particles are considered; binder is omitted, as is any conductivity enhancer, such as carbon black. Without carbon black in the model electrode, we must rely upon a percolation path within the active material in order to carry the electronic current to the current collectors. Therefore, active particles must be in direct contact with each other, and their electronic conductivity is considered as an effective conductivity of the carbon black and the solid phase. This approach certainly alters the current distribution one would find in a real battery if it could be measured.

The Li^+ diffusion coefficient for the bulk-composite $Li_xMn_2O_4$ electrode is similar to values found in the literature[1–12]; however, it should be noted that the surface area in the diffusivity calculation was an estimate. The approach used to measure the ionic conductivity of our electrolyte system is considered a standard approach, and the trend shown is similar to those reported for other electrolytes in the literature.[51,52] t_{Li+}, D_{Li+}, D_{F-} for electrolyte solutions in EC:DMC (3:7) are similar in magnitude and overall trend to measurements found in literature made on similar electrolytes.[53] It should be kept in mind that NMR measurements of t_{Li+} represent the ions in solution only, whereas the electrochemical methods are more reflective of the ions in a battery. While comparisons can be made, measurements on electrolytes are only truly valid for the electrolyte system measured; any changes to the electrolyte system will necessitate new measurement of the transference number and diffusion constant. The average particle size of the LMO material used was found to be 2.5 μm; however, the particle size distribution was large, with some particles having a diameter into the tens of microns.

Conclusions and Future Work

A new microscale model for lithium ion cells has been developed which incorporates three dimensional structure into the electrodes modeled; the anode and cathode structures are fully resolved, while the separator is treated as an effective electrolyte property. For each phase, charge and mass transport equations are formulated and solved fully coupled in the simulation; the interface condition reflecting intercalation and deintercalation is modeled by the Butler-Volmer equation. The simulation shows the expected dependence on the electrode structure and, within the limits discussed above, compares reasonably to the measurements. Therefore, in the next step, this kind of microscopic simulation can serve as a valuable tool for the study of the influence of the microstructure on cell performance. For instance, by varying the geometric parameters of the virtual electrodes (thicknesses, particle sizes porosities, etc.) battery performance can be optimized with respect to the desired design goal. Additionally, our three-dimensional simulation provides access to many local quantities like concentrations, overpotentials, interface and ion fluxes, current densities, etc., that are not easily accessible in an experiment. The analysis of those local quantities can, for example, highlight peaks of current distribution or potential, or possibly detect volume elements of the battery that are basically unused in a given application. The model cathode and electrolyte system was parameterized using values obtained from experimental results, with the exception of the reaction coefficient/proportionality factor, which was assumed to be 0.5 based on literature findings. The non-active components of the cell and the lithium foil anode were parameterized using literature values. The system used for the parameterization and subsequent validation and verification studies was a lithium manganese oxide half cell battery with a 1.2 M $LiPF_6$ in 3:7 EC:DMC electrolyte solution. The parameters measured experimentally were all similar to previously reported values for similar electrochemical systems. By experimentally determining all relevant electrochemical parameters, a self-consistent parameterization of the model was ensured.

It remains as future work to improve the resolution of the components of the electrode into active and inactive particles. This will require an imaging method which allows resolution of the varying components within a real electrode microstructure and will ultimately increase the numerical complexity of the simulation.

References

1. P. G. Dickens and G. J. Reynolds, *Solid State Ionics*, **5**, 331 (1981).
2. D. Guyomard and J. M. Tarascon, *J. Electrochem. Soc.*, **139**, 937 (1992).
3. P. Arora, B. N. Popov, and R. E. White, *J. Electrochem. Soc.*, **145**, 807 (1998).
4. S. R. Das, S. B. Majumder, and R. S. Katiyar, *J. Power Sources*, **139**, 261 (2005).
5. H. Kanoh, Q. Feng, T. Hirotsu, and K. Ooi, *J. Electrochem. Soc.*, **143**, 2610 (1996).
6. H. Kanoh, Q. Feng, Y. Miyai, and K. Ooi, *J. Electrochem. Soc.*, **142**, 702 (1995).
7. M. Nishizawa, T. Uchiyama, K. Dokko, K. Yamada, T. Matsue, and I. Uchida, *Bull. Chem. Soc. Jpn.*, **71**, 2011 (1998).
8. K. A. Striebel, C. Z. Deng, S. J. Wen, and E. J. Cairns, *J. Electrochem. Soc.*, **143**, 1821 (1996).
9. S. B. Tang, M. O. Lai, and L. Lu, *Mater. Chem. Phys.*, **111**, 149 (2008).
10. Y. Y. Xia, H. Takeshige, H. Noguchi, and M. Yoshio, *J. Power Sources*, **56**, 61 (1995).
11. D. Zhang, B. N. Popov, and R. E. White, *J. Power Sources*, **76**, 81 (1998).
12. D. Zhang, B. N. Popov, and R. E. White, *J. Electrochem. Soc.*, **147**, 831 (2000).
13. C. W. Wang and A. M. Sastry, *J. Electrochem. Soc.*, **154**, A1035 (2007).
14. R. E. Garcia and Y. M. Chiang, *J. Electrochem. Soc.*, **154**, A856 (2007).
15. X. C. Zhang, A. M. Sastry, and W. Shyy, *J. Electrochem. Soc.*, **155**, A542 (2008).
16. X. C. Zhang, W. Shyy, and A. M. Sastry, *J. Electrochem. Soc.*, **154**, A910 (2007).
17. P. Arora, R. E. White, and M. Doyle, *J. Electrochem. Soc.*, **145**, 3647 (1998).
18. M. Doyle, T. F. Fuller, and J. Newman, *J. Electrochem. Soc.*, **140**, 1526 (1993).
19. G. S. Nagarajan, J. W. Van Zee, and R. M. Spotnitz, *J. Electrochem. Soc.*, **145**, 771 (1998).
20. L. Berhan and A. M. Sastry, *Phys. Rev. E*, **75**, 041120 (2007).
21. L. Berhan and A. M. Sastry, *Phys. Rev. E*, **75**, 041121 (2007).
22. Y. H. Chen, S. D. Bakrania, M. S. Wooldridge, and A. M. Sastry, *Aerosol Sci. Technol.*, **44**, 83 (2010).
23. X. Cheng and A. M. Sastry, *Mech. Mater.*, **31**, 765 (1999).
24. X. Cheng, A. M. Sastry, and B. E. Layton, *J. Eng. Mater.-T. ASME*, **123**, 12 (2001).
25. A. M. Sastry and C. M. Lastoskie, *Philos. T. Roy. Soc. A*, **362**, 2851 (2004).
26. K. A. Striebel, A. Sierra, J. Shim, C. W. Wang, and A. M. Sastry, *J. Power Sources*, **134**, 241 (2004).
27. C. W. Wang, L. Berhan, and A. M. Sastry, *J. Eng. Mater.-T. ASME*, **122**, 450 (2000).
28. C. W. Wang, K. A. Cook, and A. M. Sastry, *J. Electrochem. Soc.*, **150**, A385 (2003).
29. C. W. Wang and A. M. Sastry, *J. Eng. Mater.-T. ASME*, **122**, 460 (2000).
30. C. W. Wang, Y. B. Yi, A. M. Sastry, J. Shim, and K. A. Striebel, *J. Electrochem. Soc.*, **151**, A1489 (2004).
31. Y. B. Yi, L. Berhan, and A. M. Sastry, *J. Appl. Phys.*, **96**, 1318 (2004).
32. Y. B. Yi and A. M. Sastry, *Physical Review E*, **66** (2002).
33. Y. B. Yi and A. M. Sastry, *Proc. R. Soc. Lond. A*, **460**, 2353 (2004).
34. Y. B. Yi, C. W. Wang, and A. M. Sastry, *J. Electrochem. Soc.*, **151**, A1292 (2004).
35. Y. B. Yi, C. W. Wang, and A. M. Sastry, *J. Eng. Mater.-T. ASME*, **128**, 73 (2006).
36. Y. H. Chen, C. W. Wang, X. Zhang, and A. M. Sastry, *J. Power Sources*, **195**, 2851 (2010).
37. W. B. Du, A. Gupta, X. C. Zhang, A. M. Sastry, and W. Shyy, *Int. J. Heat Mass Transfer*, **53**, 3552 (2010).
38. J. H. Seo, J. Park, G. Plett, and A. M. Sastry, *Electrochem. Solid St.*, **13**, A135 (2010).
39. A. Latz and S. Schmidt, in *Powders and Grains 2009*, M. Nakagawa and S. Luding Editors, p. 571 (2009).
40. A. Latz and S. Schmidt, *Granul. Matter*, **12**, 387 (2010).
41. D. Niedziela, A. Latz, and O. Iliev, *International Journal of CFD Case Studies*, **6**, 15 (2007), www.nafems.org/publications/browse_buy/cfd/cfdj6/.
42. A. Latz, U. Strautins, and D. Niedziela, *J. Non-Newtonian Fluid Mech.*, **165**, 764 (2010).
43. D. Niedziela, A. Latz, and T. Moritz, in *Simulation of Complex Flows – Applications and Trends*, Wiesbaden (2009).
44. M. Boettcher, S. Schmidt, A. Latz, M. S. Jaeger, M. Stuke, and C. Duschl, *J. Phys.-Condens. Mat.* (2010).
45. A. Latz, J. Zausch, and O. Iliev, in *Numerical Methods and Applications*, I. Dimov, S. Dimov, and N. Kolkovska Editors, p. 329 (2011).
46. A. Latz and J. Zausch, *J. Power Sources*, **196**, 3296 (2011).
47. P. Popov, Y. Vutov, S. Margenov, and O. Iliev, in *Numerical Methods and Applications*, I. Dimov, S. Dimov, and N. Kolkovska Editors, p. 338 (2011).
48. C. J. Wen, B. A. Boukamp, R. A. Huggins, and W. Weppner, *J. Electrochem. Soc.*, **126**, 2258 (1979).
49. W. Weppner and R. A. Huggins, *J. Electrochem. Soc.*, **124**, 1569 (1977).
50. C. Ho, I. D. Raistrick, and R. A. Huggins, *J. Electrochem. Soc.*, **127**, 343 (1980).
51. X. L. Wang, L. Z. Fan, Z. H. Xu, Y. H. Lin, and C. W. Nan, *Solid State Ionics*, **179**, 1310 (2008).
52. N. Nanbu, S. Watanabe, M. Takehara, M. Ue, and Y. Sasaki, *J. Electroanal. Chem.*, **625**, 7 (2009).
53. C. Capiglia, Y. Saito, H. Kageyama, P. Mustarelli, T. Iwamoto, T. Tabuchi, and H. Tukamoto, *J. Power Sources*, **81**, 859 (1999).
54. D. R. Lide, *CRC Handbook of Chemistry and Physics*, CRC Press, Boca Raton (1995).
55. Celgard, Celgard Product Comparison – http://www.celgard.com/pdf/library/Celgard_Product_Comparison_10002.pdf, in, Celgard, Charlotte (2009).